Shear-resistant topology in the quasi-one-dimensional van der Waals material Bi_4Br_4

Jonathan K. Hofmann,[1,2,3,*] Hoyeon Jeon,[4] Saban M. Hus,[4] Yuqi Zhang,[5,6,7] Mingqian Zheng,[8] Tobias Wichmann,[1,2,3] An-Ping Li,[4] Jin-Jian Zhou,[8] Zhiwei Wang,[5,6,7] Yugui Yao,[5,6,7] Bert Voigtländer,[1,2,3] F. Stefan Tautz,[1,2,3] and Felix Lüpke[1,2,9,†]

[1]*Peter Grünberg Institute (PGI-3), Forschungszentrum Jülich, 52425 Jülich, Germany*
[2]*Jülich Aachen Research Alliance (JARA), Fundamental of Future Information Technology, 52425 Jülich, Germany*
[3]*Institute for Experimental Physics IV A, RWTH Aachen University, Otto-Blumenthal-Straße, 52074 Aachen, Germany*
[4]*Center for Nanophase Materials Sciences, Oak Ridge National Laboratory, Oak Ridge, Tennessee, USA*
[5]*Key Laboratory of Advanced Optoelectronic Quantum Architecture and Measurement, Ministry of Education, School of Physics, Beijing Institute of Technology, Beijing 100081, China*
[6]*Beijing Key Lab of Nanophotonics and Ultrafine Optoelectronic Systems, Beijing Institute of Technology, Beijing 100081, China*
[7]*International Center for Quantum Materials, Beijing Institute of Technology, Zhuhai 319000, China*
[8]*Centre for Quantum Physics, Key Laboratory of Advanced Optoelectronic Quantum Architecture and Measurement (MOE), School of Physics, Beijing Institute of Technology, Beijing 100081, China*
[9]*Institute of Physics II, Universität zu Köln, Zülpicher Straße 77, 50937 Köln, Germany*

(Received 25 November 2024; revised 10 May 2025; accepted 22 May 2025; published 12 June 2025)

Bi_4Br_4 is a prototypical quasi-one-dimensional (1D) material in which covalently bonded bismuth bromide chains are arranged in parallel, side-by-side and layer-by-layer, with van der Waals (vdW) gaps in between. So far, two different structures have been reported for this compound, α-Bi_4Br_4 and β-Bi_4Br_4, in both of which neighboring chains are shifted by $\mathbf{b}/2$, i.e., half a unit-cell vector in the plane, but which differ in their vertical stacking. While the different layer stacking is known to result in distinct electronic properties—higher-order and weak topological insulators, respectively—the effect of different in-plane arrangements of the atomic chains remains an open question. Here, using scanning tunneling microscopy and spectroscopy (STM/STS), we report an unusual $Bi_4Br_4(001)$ structure, with a shift of $\mathbf{b}/3$ between neighboring chains in the plane and AB layer stacking. We determine shear strain to be the origin of this structure, which can readily result in shifts of neighboring atomic chains because of the weak interchain bonding. For the observed $b/3$ structure, the (residual) atomic chain shift corresponds to an in-plane shear strain of $\gamma \approx 7.5\%$. STS reveals a bulk insulating gap and metallic edge states at monolayer surface steps, indicating that, just like for α-Bi_4Br_4, monolayers of the $b/3$ structure are also quantum spin Hall insulators, in agreement with density functional theory (DFT) calculations.

DOI: 10.1103/tdp5-wmqc

I. INTRODUCTION

The quasi-1D vdW materials Bi_4X_4, where X = (Br, I), have attracted recent interest, because, among other aspects, their nontrivial band topologies realize exotic electronic properties [1–3]. Monolayer Bi_4Br_4 was identified both in theory and experiment to be a quantum spin Hall (QSH) insulator [4–7], manifesting in an insulating 2D interior and gapless helically spin-polarized edge states [8,9], with potential applications in spintronics and quantum computing [10]. These properties are maintained for a monolayer of Bi_4Br_4 on a bulk α-Bi_4Br_4 substrate, without significantly altering its QSH properties [4,5]. As a result, along step edges of the monolayer, topologically protected edge states were observed, which persisted from 4.2 K up to room temperature [11].

Bulk α-Bi_4Br_4 is a higher-order topological insulator (HOTI): Along lines ("hinges") where certain surface facets meet, e.g., (100) and (001) in the case of Bi_4Br_4, topologically protected so-called hinge states can exist. These hinge states are one-dimensional states extending along the (step) edge between two facets [11–15]. Bulk α-Bi_4Br_4 can be thought of as a stack of multiple individual monolayers, each of which would be a QSH insulator with edge states. However, because of the AB stacking of α-Bi_4Br_4, pairs of QSH edge states in adjacent layers interact in a way that is specific for the orientation of the side facet. This is illustrated in the atomic model of a α-Bi_4Br_4 unit cell in Fig. 1(a) for a stack of two monolayers. On the right ([100] facet), where the two chains meet at an obtuse angle $<180°$, the two edge states hybridize [14]. In contrast, on the left ([$\bar{1}$00] facet), where the chains meet at an angle $>180°$ and consequently the two edge states are separated by protruding atoms in both chains, they do not hybridize, forming instead two separate hinge states at

*Contact author: jo.hofmann@fz-juelich.de
†Contact author: f.luepke@fz-juelich.de

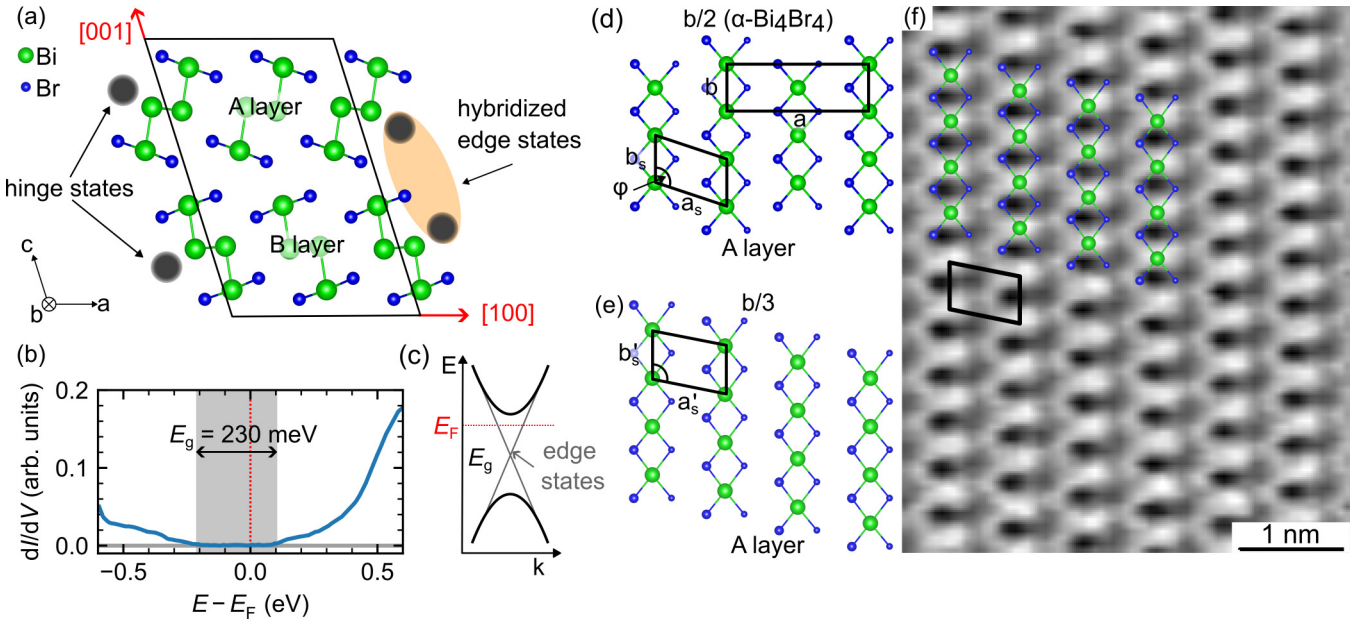

FIG. 1. (a) Atomic model of α-Bi_4Br_4, with AB layer stacking. The black line shows a projection of the monoclinic bulk unit cell. Each monolayer is a quantum spin Hall (QSH) insulator with edge states (gray circles). On the right, the edge states hybridize, while on the left, they form two hinge states. See the main text for more details. (b) Scanning tunneling spectrum of the $b/3$ surface with band gap E_g, measured at the set point $V_t = 0.6$ V and $I_t = 50$ pA. (c) Schematic band structure with topological gap and edge states. (d) Top-view of the α-Bi_4Br_4(001)-A surface. The lower Br atoms are indicated by smaller size. Neighboring chains are shifted by $\mathbf{b}/2$ with respect to each other. The rectangle shows the projected monoclinic bulk unit cell (which equals the nonprimitive centered surface unit cell), the parallelogram is the primitive surface unit cell. (e) The experimentally observed surface structure in which neighboring chains are shifted by $\mathbf{b}/3$ against each other. The primitive surface unit cell is shown. (f) STM topography recorded at $I_t = 0.4$ nA and $V_t = -0.4$ V. The atomic model from (e) is superimposed on the chains, showing good agreement. The image has been upscaled by linear interpolation. The spectrum displayed in (b) was smoothed using a moving average with a 14-meV window.

the top and the bottom of the stack [11]. The name hinge state becomes clearer if one considers four- or six-monolayer stacks, where the edge states hybridize as discussed above, leaving one state at the top of the stack as a hinge between the [100] and [001] facets, and another one at the bottom and on the same side of the stack as a hinge between the [100] and [00$\bar{1}$] facets, cf. the schematic drawings, which illustrate the systematics of hinge states on terraces with (001) orientation displayed in Sec. S1 within the Supplemental Material [16]. This schematics also makes it clear that the edge-state properties depend on the stacking arrangement of the layers. However, the influence of (hypothetical) shifts along the chains, i.e., the stacking of the chains in the in-plane layer, is not clear at present.

In this paper, we report an unusual structure of the α-Bi_4Br_4(001) surface. In high-resolution STM topography images, we observe a shift of $\mathbf{b}/3$ between neighboring chains (in at least the top two layers of the sample) and propose a corresponding crystal structure. Analyzing the STM topography of terraces separated by monolayer steps, we observe AB stacking, as present in α-Bi_4Br_4, despite the structural modification within the planes. Experimental spectra taken at monolayer step edges and results from our density functional theory (DFT) calculations confirm the existence of QSH edge states in the $b/3$ monolayer.

Before turning to our results, we briefly summarize the crystal structure of α-Bi_4Br_4. It crystallizes in a base-centered monoclinic structure with space group C2/m [18]. The lattice constants are $a = 1.3064$ nm, $b = 0.4338$ nm, $c = 2.0061$ nm, and $\sphericalangle ac \equiv \beta = 107.42^\circ$ [18]. Figure 1(a) shows an atomic model of the monoclinic unit cell of α-Bi_4Br_4 projected along the b axis, while Fig. 1(d) displays a top view of the α-Bi_4Br_4(001) surface. The Bi atoms (green) form short, four-membered and S-shaped units in the ac plane, with four Br atoms (blue) each, two of which are bonded to the top and two of which are bonded to the bottom Bi atoms. These Br atoms connect the S-shaped Bi units into infinite chains that extend in the $\mathbf{b}$ direction, cf. Fig. 1(d). Since all interchain bonds are of vdW type, α-Bi_4Br_4 can be classified as a quasi-one-dimensional vdW crystal. In Fig. 1(d) both the projected bulk unit cell, which maps onto a centered rectangular surface unit cell, and the primitive surface unit cell (parallelogram) of the α-Bi_4Br_4(001) surface are indicated. The primitive unit cell is spanned by lattice vectors $\mathbf{b}_s$ (with $\mathbf{b}_s = \mathbf{b}$) and $\mathbf{a}_s$ with length $a_s = \sqrt{(a/2)^2 + (b/2)^2} = 0.688$ nm. The angle between these lattice vectors is $\varphi = 108.4^\circ$. The interchain distance d between two neighboring chains is given by $d = a/2 = 0.6532$ nm. As can be seen in Fig. 1(a), α-Bi_4Br_4 exhibits AB stacking along the c axis, with chains of S- and $\mathfrak{Z}$-shaped cross section stacked on top of each other. Because of the AB stacking, the (001) surface can expose either an A or a B layer. In the projection of Fig. 1(a), the layers are distinguished by the topmost Br atom being placed either to the left (A) or to the right (B) of the Bi atom [11,15]. The top view in Fig. 1(d) shows the A surface, the lower-lying Br atoms are indicated by a smaller diameter. The

A-to-A or B-to-B step height is equal to the height of the unit cell, $h = c \sin\beta = 1.91$ nm. Therefore, the step height from A to B (or B to A) is 0.96 nm. Note that neighboring atomic chains on the α-$Bi_4Br_4(001)$ surface are shifted by $\mathbf{b}/2$ with respect to each other [cf. Fig. 1(d)]. This can be clearly seen in the rectangular unit cell spanned by the lattice vectors **a** and **b**.

II. METHODS

The α-Bi_4Br_4 single crystal, grown by the self-flux method [14], was glued to a standard sample plate using conductive epoxy. The sample was then introduced into UHV, where it was cleaved at room temperature using Kapton tape, which was peeled off along the **b** direction.

Experiments were carried out in the low-temperature four-tip scanning tunneling microscope (STM) in Oak Ridge at 4.7 K using a commercial PtIr tip. Scanning tunneling spectroscopy (STS) was performed with a lock-in amplifier, employing a modulation frequency $f = 500$ Hz and modulation amplitudes $V_{\mathrm{mod}} = 10$ mV to 100 mV. Figure 1(b) shows a scanning tunneling spectrum of the α-Bi_4Br_4 crystal used in this study (with the $b/3$ structure), showing properties consistent with the literature. The bulk band gap is $E_g = 230(40)$ meV, as estimated from multiple spectra using the method described in Ref. [19] (compare also Sec. S4 within the Supplemental Material [16]). This value falls into the range of experimentally measured band gaps of α-Bi_4Br_4 reported in the literature ($b/2$ structure), either from ARPES (0.3 eV [13] and 0.23 eV [7]), STS (0.26 eV [11,15] and ~0.2 eV [7]), or optical measurements (0.22 eV) [6]. A schematic sketch of the band structure is depicted in Fig. 1(c).

Density functional theory (DFT) calculations were carried out to investigate the electronic properties and topological band character of Bi_4Br_4 monolayers, both in the well-known $b/2$ and the $b/3$ structures. We employed the Vienna *ab-initio* simulation package (VASP) [20] with the Heyd–Scuseria–Ernzerhof hybrid functional (HSE06) [21] to describe the exchange-correlation potential, and set the energy cutoff of the plane-wave basis to 300 eV. To construct maximally localized Wannier functions for the p orbitals of Bi and Br atoms, we used the WANNIER90 code [22] and performed the calculations on a $6 \times 6 \times 3$ k mesh. Relaxing the Bi_4Br_4 monolayer structure did not lead to crystal structures that are compatible with the experimental structures, which we tentatively assign to the difficulty of describing vdW interactions in DFT. Therefore, we fixed the unit cells for the calculations according to the literature and experimental data, respectively, without further relaxation.

A second set of DFT calculations was carried out to analyze the total energies (per unit cell) as a function of the shift between neighboring Bi_4Br_4 chains in the monolayer structure. In these calculations, we used the experimentally determined crystal structure of monolayer Bi_4Br_4 [18]. Periodic boundary conditions with a 2-nm vacuum gap between monolayers were employed. The chains were shifted rigidly against each other, without relaxation from their bulk structure in α-Bi_4Br_4. The calculations were performed with a plane-wave basis set as implemented in Quantum ESPRESSO [23,24]. We used the generalized gradient approximation (GGA) with the Perdew-Burke-Ernzerhof (PBE) [25] exchange-correlation functional. Further, we employed scalar relativistic projector augmented wave (PAW) pseudopotentials, generated using an "atomic" code [26] with a nonlinear core correction; semicore d electrons were treated as valence electrons. The DFT-D3(BJ) vdW correction [27] was used to account for the vdW interactions. The plane-wave cutoff energies for the electronic wave functions and the charge density were set to 60 and 720 Ry, respectively, and the energy convergence criterion was set to 10^{-9} Ry. A $8 \times 8 \times 2$ Monkhorst-Pack grid was chosen for k-point sampling. Convergence was verified for the $b/2$-, $b/3$- and 0-shifted geometries.

III. EXPERIMENTAL RESULTS

A. Surface structure

Figure 1(f) shows an atomically resolved STM topography image of the $Bi_4Br_4(001)$ surface. It clearly shows parallel chains, running along the b axis (from top to bottom in the image). However, the mutual alignment of these chains does not correspond to the bulk-terminated α-$Bi_4Br_4(001)$ surface: Instead of the expected $s = b/2$ offset [cf. Fig. 1(d)] that was already observed in the literature [7,11,15,28], the image reveals a shift of $s = b/3$ between neighboring chains. This structure is no longer spanned by the two surface lattice vectors $\mathbf{a}_s$ and $\mathbf{b}_s$, but by the new lattice vectors $\mathbf{a}_s'$ and $\mathbf{b}_s'$ displayed in Fig. 1(e). From Fig. 1(f), we extract the lengths of the lattice vectors as $a_s' = 0.69(4)$ nm and $b_s' = 0.45(3)$ nm with an angle $\varphi' = 101(5)^\circ$ between them; the interchain distance is determined as $d' = 0.68(4)$ nm. These values are averages obtained from multiple STM topographs, including Figs. 1(f) and 2. We note that although the lattice vector $\mathbf{b}_s'$ appears slightly larger than that of α-phase Bi_4Br_4 ($b_s = 0.4338$ nm [18]), both still coincide within the experimental error of b_s', i.e., $b_s' \approx b_s$. Superimposed on the STM topography in Fig. 1(f), a model of the $b/3$ structure based on rigidly shifted chains shows good agreement with the experimental image. The positions of the individual atoms on the surface were identified by comparison with annotated STM topographies in Ref. [11] and DFT calculations [7,28], which show that the deeper depression in the surface topography appears near the more elevated Br atoms. The shift of the adjacent chains results in a shear strain $\gamma = (b/2 - s)/d$, which for $s = b/3$ results in $\gamma \approx 7.5\%$ strain with respect to the $b/2$ structure.

For several reasons, scan distortions can be excluded as the origin of the $b/3$ structure. First, before the experiments on Bi_4Br_4, we carefully calibrated the STM on the Au(111) surface (Fig. S2 within the Supplemental Material [16]). Second, the fact that the structure is consistent both within one image and between multiple scans of the same area rules out piezo creep and drift (Fig. S3 within the Supplemental Material [16]). Third, on terraces separated by a monolayer step the same structure rotated by 180° is observed as we will now show.

On the $Bi_4Br_4(001)$ surface, we observed multiple parallel steps running in the $\mathbf{b}_s'$ direction. Figure 2(a) shows a high-resolution STM topography of such a step. From the height

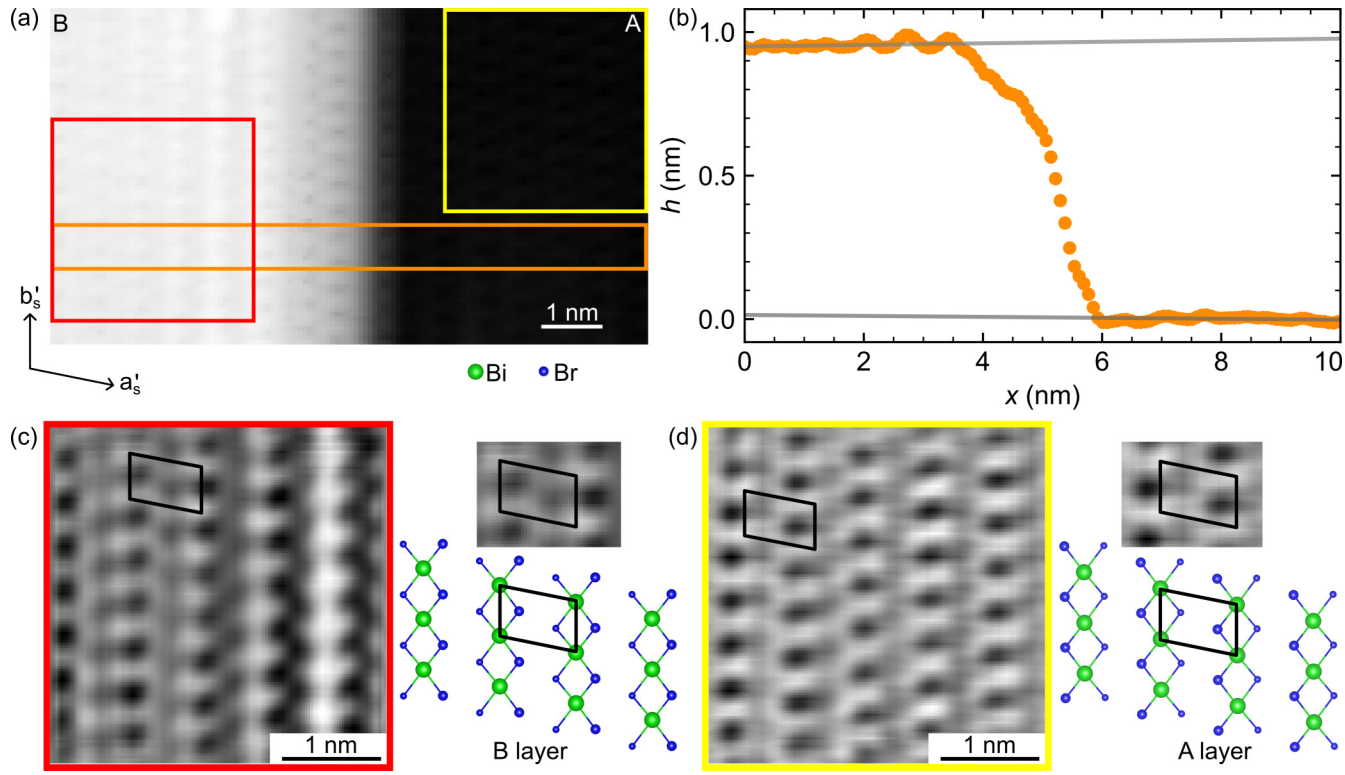

FIG. 2. (a) STM topography of a step edge on the $Bi_4Br_4(001)$ surface, acquired at $I_t = 0.1$ nA and $V_t = -0.3$ V. The image shows a one-monolayer step edge with atomic resolution on both the upper and the lower terraces. (b) Line profile indicated by the orange box in (a). (c) and (d) show a zoom-in of the upper and the lower terraces, respectively. In panel (d), the surface structure can be readily identified by comparing to Fig. 1(f) and the literature [11]: The lower terrace presents the A surface. In panel (c), a standing wave originating from the step edge is imposed onto the atomic resolution on the upper terrace. Nevertheless, away from the step edge, the lattice is identified as a B surface. For comparison, we also show the unit cell together with ball-and-stick models of the corresponding surfaces. The detail images have been scaled up using linear interpolation and denoised using Fourier filtering.

profile displayed in Fig. 2(b), a step height of 0.97 nm can be extracted. This step height compares well with experimental step heights reported in the literature [7,11]. According to the crystal model in Fig. 1(a), on α-$Bi_4Br_4(001)$ a step height of 0.96 nm corresponds to a change from an A to a B surface or vice versa.

To check whether AB stacking is also observed for the $b/3$ structure, we zoom into the upper and lower terraces next to the step [Figs. 2(c) and 2(d)]. On the lower terrace, we readily observe the A surface, as defined in Fig. 1. On the upper terrace, there is a strong modulation of the topographic height next to the step edge [compare also the line profile in Fig. 2(b)], which we attribute to a standing wave pattern originating from the step edge. The standing wave partially masks the atomic resolution on the upper terrace, but nevertheless, the upper terrace can be identified as a B terrace. Consequently, AB stacking is also present in the $b/3$ structure. From this, we can also exclude that we have observed β-Bi_4Br_4, as this polymorph of Bi_4Br_4 is expected to feature AA stacking [29].

B. Electronic structure

We now turn to the electronic properties of the $b/3$ structure. Figure 3(a) shows two parallel steps that together form a trench of one monolayer depth on the surface with $b/3$ structure. As explained above, for the $b/2$ structure, we expect the presence of topologically protected edge states at the steps, as schematically indicated in Fig. 3(b). The question is whether such edge states are also present in the $b/3$ structure. Figures 3(c) and 3(d) display scanning tunneling spectra taken along lines across the two step edges. In both measurements, the bulk band gap is clearly visible away from the steps. However, at the step edges, we observe a localized density of states (LDOS) within the band gap, which extends 2 to 3 nm into the top terraces (compare Ref. [11])—a typical signature of topological edge states [19,30,31] and similar to literature reports for the $b/2$ structure [6,7,11,15]. For a more detailed comparison, we plot the averages of the three distinct regions for each step (upper terrace, edge, lower terrace) in Figs. 3(e)–(g). We interpret the nonvanishing LDOS of the $b/3$ structure within the bulk band gap as arising from the QSH edge states that are expected for a monolayer step on the α-$Bi_4Br_4(001)$ surface (see Sec. S1 of the Supplemental Material [16]). We thus conclude that a Bi_4Br_4 monolayer in the $b/3$ structure also is a QSH insulator.

It is well known that the precise location of hinge states in α-Bi_4Br_4 depends on the step height [11,14,15]. Considering a trench with the same step height on both sides, as in the present case, there will always be two hinge states no matter which facets [(100), $(\bar{1}00)$, $(10\bar{1})$, or $(\bar{1}01)$] form the walls of the trench. For a step height corresponding to an even number

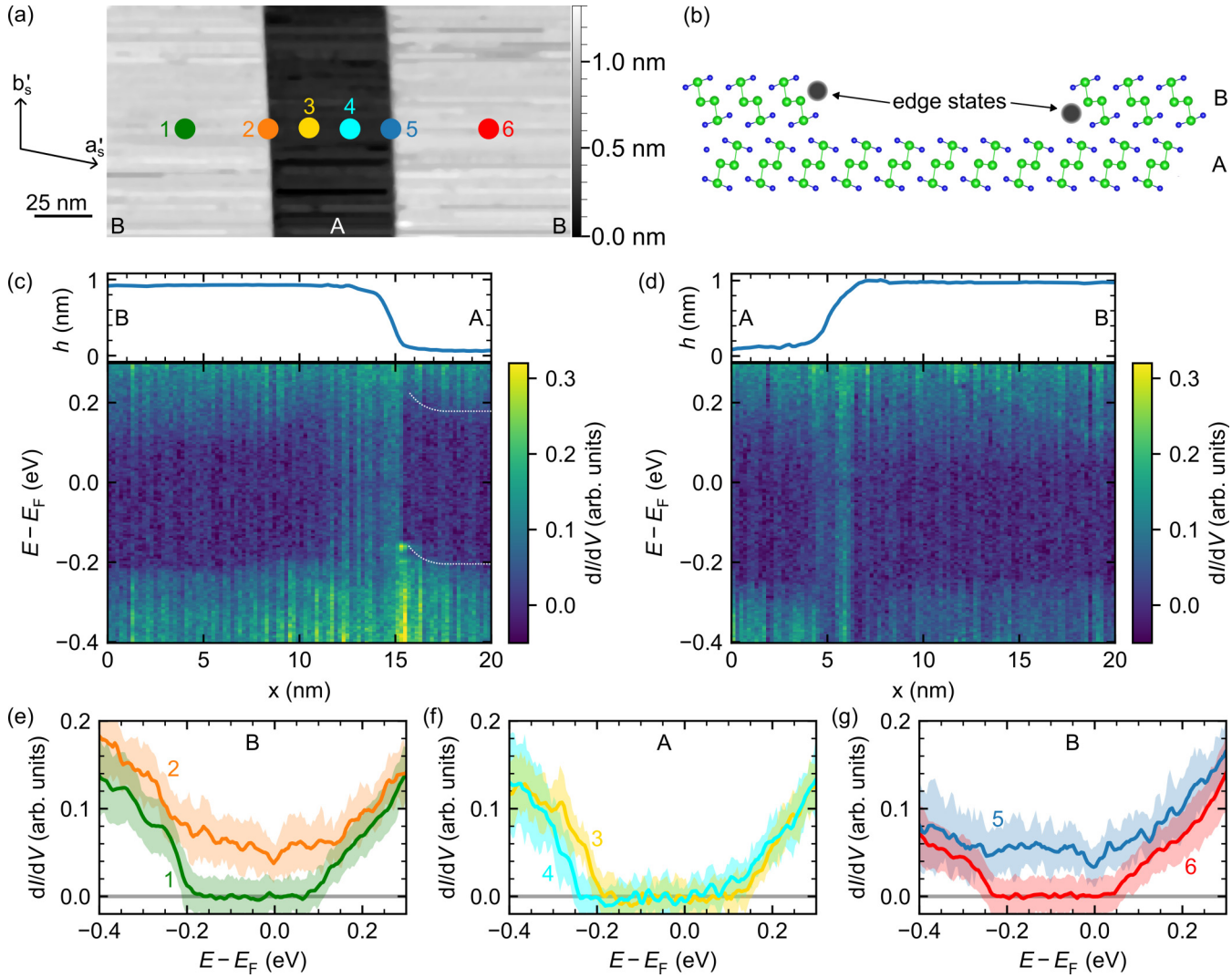

FIG. 3. (a) STM topography of a trench in the surface, bordered by two Bi_4Br_4 monolayer steps. (b) Atomic model of the trench with indicated edge states [filled circles, according to Fig. 1(a)]. (c) and (d) show the topography and tunneling spectra taken along lines crossing the left (c) and right (d) step edge, respectively. The spectra exhibit the bulk band gap away from the steps and a metallic density of states located at the topographic step edge, extending into the respective upper terraces. The dotted white lines in (c) mark the band bending close to the edge on the lower terrace. Panels (e)–(g) show averaged spectra of sections of (c) and (d), with filled circles in (a) schematically indicating the locations of the spectra. Spectrum 2 and 5 show metallic edge states within the bulk band gap. The spectra have been smoothed using a moving average with a 14-meV window. The shaded areas indicate the standard deviation.

of layers, the two hinge states appear on the same step on one side of the trench. In contrast, for an odd number of layers, they are located at opposite sides, cf. Sec. S1 within the Supplemental Material [16] and Refs. [11,14,15]. Thus, if the step height corresponds to a single layer on both sides of the trench, we expect hinge states, i.e., quantum spin Hall edge state in this case, on both sides of the trench [Fig. 3(b)]. Thus, the electronic structures shown in Figs. 3(e)–(g) are consistent with the step height of one monolayer. We note, however, that the edge configuration and thus also the details of the edge state localization differ for the two steps, i.e., for the left step in Fig. 3(b) the edge state is more localized at the top of the step, whereas at the right step it is more localized at the bottom of the step [11]. This difference may explain our observed different edge state signatures in Figs. 3(c)–(g). We further note that slight shifts between the curves in panel (e) through (g) may be the result of defects [28], which may also give rise to a slight band bending [32], which we observe close to the step edge in panel (c).

We now analyze with DFT whether the $b/3$ structure is expected to be a QSH insulator. It is well known that DFT predicts the Bi_4Br_4 monolayer in the $b/2$ structure to be a QSH insulator [4,5]. For the $b/2$ structure, the QSH property arises from the inverted band gap at the Y point that is caused by the spin-orbit coupling (SOC). The latter exchanges the two Bi-6p orbitals from which the lowest conduction band and the highest valence band derive. Crucially, this also leads to the exchange of parity between the conduction and valence bands at the Y point [Figs. 4(a) and 4(b)], which makes the $b/2$ structure a QSH insulator.

Since the experimentally determined interchain distance d' and the surface lattice vector $\mathbf{b}'_s$ of the $b/3$ structure are

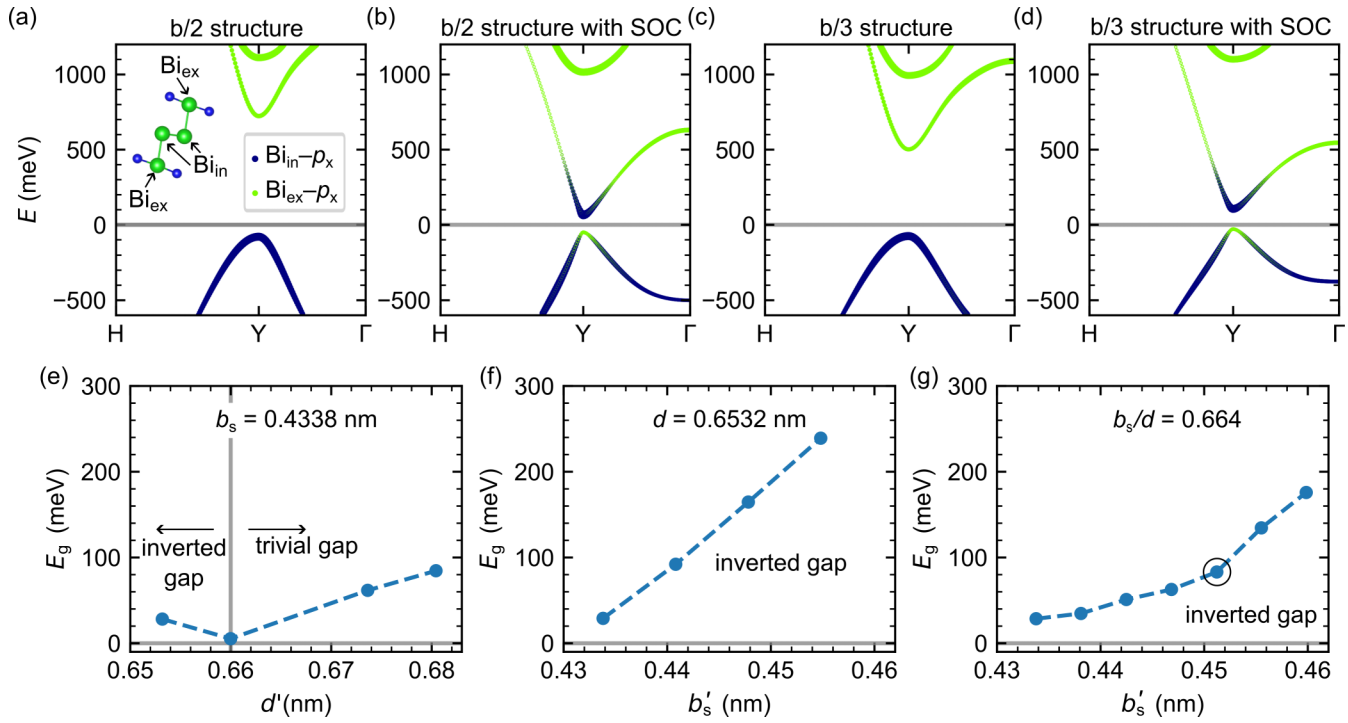

FIG. 4. (a) and (b) show the Bi_{in}-p_x and Bi_{ex}-p_x projected orbital character of the conduction and the valence bands around the Y point without (a) and with (b) SOC for the $b/2$ structure, see [4]. (c) and (d) show the same projected orbital character of the bands around the Y point for the $b/3$ structure. (c) and (d) were calculated using the lattice constants indicated in the main text. For both structures, SOC exchanges the two orbitals leading to an exchange of parity, which makes both the $b/2$ (b) and the $b/3$ (d) structure a QSH insulator. (e)–(g) Evolution of the inverted band gap E_g as a function of the interchain distance d' and the lattice constant $b_{S'}$. The dashed lines are a guide for the eyes. (e) Dependence of E_g on the interchain distance d', when fixing $b_S = 0.4338$ nm. The inverted band gap decreases, until it closes at $d' = 0.66$ nm, and then transitions to a trivial gap. (f) Fixing $d = 0.6532$ nm and increasing the lattice vector $b_{S'}$ enhances the inverted band gap. (g) The same applies if the ratio $b_s/d = 0.664$ is kept constant.

somewhat larger than the literature values for α-Bi_4Br_4, and since it is evident that these structural parameters must have a strong influence on the band structure, we investigated the evolution of the band gap with d' and b'_s. Figure 4(e) displays the dependence of the nature and size of the band gap of the $b/3$ structure on d' when b'_s is fixed to the literature value of the $b/2$ structure, $b_s = 0.4338$ nm. We find that the $b/3$ structure becomes a trivial insulator for $d' > 0.66$ nm. Since this threshold still lies within the error bars of the experimentally determined value $d' = 0.68(4)$ nm, the DFT result is compatible with the $b/3$ structure indeed being a QSH insulator. We note that the interchain distance of the $b/2$ structure ($d = 0.653$ nm) is well below the threshold of 0.66 nm. However, the experimental b'_s is larger than the literature value b_s for the $b/2$ structure. Therefore, we also investigate the dependence of the topological properties on b'_s. To this end, we fix d' at $d = 0.6532$ nm, i.e., the value for the $b/2$ structure, and increase b'_s, starting from its literature value for the $b/2$ structure ($b_s = 0.4338$ nm). The result is displayed in Fig. 4(f). It shows that stretching b'_s has the opposite effect of stretching d', i.e., a larger b'_s stabilizes the QSH property by increasing the inverted gap, and that this effect is significant. It should stabilize the nontrivial topological properties of the $b/3$ structure with its larger b'_s even further.

The opposite scaling behavior of topological properties with d' and $b_{S'}$ raises the question which of these two effects is stronger. Therefore, we investigated the nature and size of the gap as both parameters, d' and b'_s, are increased simultaneously, such that their ratio is constant (clearly, this also requires a scaling of a'_s). Since—interestingly—this ratio is nearly identical for the $b/2$ and $b/3$ structures ($b'_s/d' = 0.662$ and $b_s/d = 0.664$), we fixed the ratio to 0.664. The result is plotted in Fig. 4(g). In the complete range, the gap is inverted and the $b/3$ structure is a QSH insulator, with the gap opening further with increasing b'_s. Hence, the larger experimental value of $b'_s > b_s$ stabilizes the QSH insulator gap, even if the mutual displacement along $\mathbf{b}_s$ in the $b/3$ structure is expected to lead to an increased (and destabilizing) $d' > d$ for steric reasons (stronger repulsion between Br atoms).

Alternatively, one can take the view that a change in b_s from the $b/2$ to the $b/3$ is unlikely, since this lattice constant is determined by covalent bonds. In that case, we define $b'_s \equiv b_s = 0.4338$ nm and scale the experimentally measured a'_s and d' accordingly [assuming an isotropic distortion of the experimental image in Fig. 1(f)], obtaining $\tilde{a}'_s = 0.67(4)$ nm and $\tilde{d}' = 0.66(4)$. The latter value is close to the calculated threshold for a nontrivial topology ($d' = 0.66$), but given the experimental error, the result is once more compatible with the $b/3$ structure being a QSH insulator, although again with a slightly smaller topological gap than the $b/2$ structure.

From the structures represented in Fig. 4(g), we find the closest agreement with the experimental parameter set [$a'_s = 0.69(4)$ nm, $b'_s = 0.45(3)$ nm, $d' = 0.68(4)$ nm, and

$\varphi' = 101(5)^\circ$] for the marked data point, with calculated parameters $a'_{s,c} = 0.6959\,\text{nm}$, $b'_{s,c} = 0.4512\,\text{nm}$, $d'_c = 0.6795\,\text{nm}$, $\varphi'_c = 102.48^\circ$. For this model of the $b/3$ structure, the energy gap is predicted to be $E_G = 80\,\text{meV}$. This is smaller than the gap DFT-predicted gap of the $b/2$ structure ($E_g = 100\,\text{meV}$). However, it should be noted in this context that DFT generally tends to underestimate band gaps. For the $b/2$ structure, experimentally determined gaps are in the range 200 meV to 300 meV; for STS measurements on the surface of a bulk α-Bi_4Br_4 crystal in the $b/2$ structure $E_g = 260\,\text{meV}$ has been reported [11,15]. In our STM experiments, we observe a slightly smaller gap of $E_G = 230(40)$ meV. This is line with a slightly smaller DFT-predicted gap of the $b/3$ structure when compared with the $b/2$ structure, suggesting that the former is somewhat closer to the transition to trivial topology. Figures 4(c) and 4(d) show Bi_{in}-p_x and Bi_{ex}-p_x orbital projected character of bands without and with SOC, respectively, in analogy to Figs. 4(a) and 4(b) for the $b/2$ structure. Also for the $b/3$ structure, the SOC leads to a change in parity at the Y point. To substantiate this conclusion, we performed additional edge state and Wilson loop calculations, which result in $\mathbb{Z}_2 = 1$ (see Sec. S5 within the Supplemental Material [16]). We therefore finally conclude that the $b/3$ structure is a QSH insulator.

IV. DISCUSSION

We now turn to a discussion of the origin of the observed $b/3$ structure, which has not been reported in the literature so far. Since STM only allows access to the topmost layer, we cannot directly determine if the $b/3$ crystal structure is present deeper in the sample or only at its surface. However, since we observe the $b/3$ lattice to be present across step edges (i.e., on adjacent surface terraces), we conclude that either only the topmost layer systematically exhibits a $b/3$ structure (surface reconstruction), or that *at least* the top two monolayers of our sample are in the $b/3$ structure. A surface reconstruction is rendered unlikely by the fact that other groups have consistently observed the $b/2$ structure at the surface [7,11,15,28]. Furthermore, the possibility of a surface reconstruction is also essentially ruled out by DFT calculations.

Figure 5 displays the total energy ΔE_{tot} per monolayer unit cell as a function of the shift s in units of b, referenced to E_{tot} of the $b/2$ structure. Also shown is the dependence on the angle φ between the two primitive unit cell vectors $\mathbf{a}_s$ and $\mathbf{b}_s$. Evidently, the $b/2$ structure ($s = b/2$ and $\varphi = 108.4^\circ$) represents an energetic minimum, with the total energy increasing monotonically towards the $b/3$ structure with $s = b/3$ and $\varphi' = 102^\circ$. The energetically least favorable configuration is $s = 0$ ($\varphi' = 90^\circ$). Overall, the behavior in Fig. 5 can be understood as the result of steric hindrance between atoms in neighboring chains. While these results suggest that the $b/3$ structure is not energetically favorable and does not even correspond to a local energy minimum, it should be kept in mind that the DFT calculations were carried out for a single Bi_4Br_4 monolayer of the bulk structure and without relaxation of the internal chain structure or the experimental interchain distance. In principle, intrachain distortions could stabilize the $b/3$ structure; however, we consider it unlikely that the total energy increase of 0.3 eV per unit cell (Fig. 5) could be offset by such distortions. Thus, we reject the possibility of a reconstruction that leads to an energy minimization of the crystal structure. This leaves us with the scenario of external stress distorting the crystal structure.

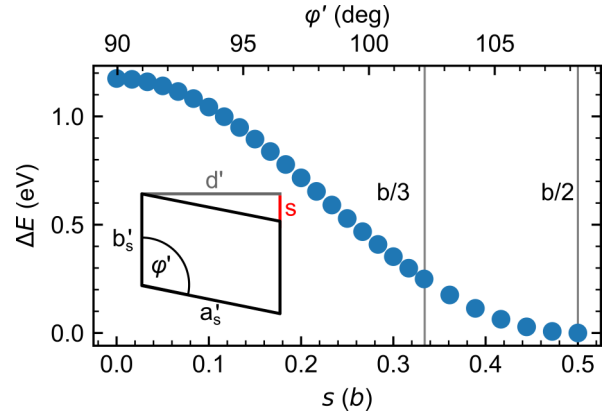

FIG. 5. Total energy per unit cell relative to the $b/2$ structure as a function of the shift $s = -d\cot\varphi$ (plotted in units of b) between neighboring chains, where d is the interchain distance. φ is the angle between the constant unit cell vector $\mathbf{b}_s$ and the changing $\mathbf{a}_s$ associated with s. The inset defines φ', d', s, a'_s, and b'_s.

Because of the quasi-1D nature of α-Bi_4Br_4, it is conceivable that especially externally applied shear stress will result in distortions of the crystal structure. For example, it is well known that external stress applied parallel to the planes of 2D vdW materials can result in glide shifts of the crystal planes and significantly modifies their electronic structure [33]. Since in quasi-1D vdW materials the in-plane shear modulus is much smaller than in 2D compounds, because of the additional vdW gaps in the 2D plane, glide shifts of the chains are easily conceivable. We note that the function $\Delta E_{tot}(s)$ (Fig. 5), by symmetry, is periodic $\Delta E_{tot}(s) = \Delta E_{tot}(s - b)$. Because of the periodicity of $\Delta E_{tot}(s)$, the maximum shear strain $\gamma = (b/2 - 0)/d = 33\%$ occurs at $\varphi' = 90^\circ$, i.e., when neighboring chains are aligned and $s = 0$. This means that a strain that would lead to $s > b$ (even $s \gg b$) causes a plastic deformation with neighboring chains shifting against each other by one or more lattice constants b. Owing to the translational symmetry of the crystal, we can only detect this residual strain corresponding to $s \bmod b/2$. In this strained crystal scenario, there is *a priori* no reason why the residual strain should lock at any particular value of s, e.g., $s = 1/3$ (corresponding to the $b/3$ structure and $\gamma \approx 7.5\%$) as in the present case. However, it should be noted that small relaxations of the internal chain structure could occur as the response to an external stress, such that the *intra*chain interaction energy could make certain values of s metastable.

The strain-based explanation of the $b/3$ structure raises the question of the origin of the stress. Here, three possibilities are conceivable. First, stress could have been applied when handling the bulk crystal, e.g., when gluing it on the STM sample holder. In this case, we would expect the $b/3$ structure to extend throughout most of the sample. Second, the strain could have been introduced during the cleaving process of the sample in UHV. Note that we cleaved the sample approximately in the **b** direction, such that a small misalignment of

the pulling direction from **b** may well explain the observed strain. In both of these scenarios, we expect the strain field to extend through the sample on macroscopic length scales. Third, microscopic inhomogeneities in the bulk crystal, such as mosaic spread or domain boundaries could induce stress within individual domains. However, in our experiments we observed the $b/3$ structure throughout the whole investigated area, such that we deem the latter explanation unlikely.

V. CONCLUSIONS

We report an unusual monolayer structure of Bi_4Br_4 in which the shift between quasi-1D chains is $b/3$ instead of $b/2$. We exclude the possibility of a surface reconstruction and conclude that it likely results from external shear stress. The resulting gliding of the quasi-1D chains against each other does not change the AB layer stacking of the original α-Bi_4Br_4 crystal. Experimentally, we find strong evidence that the $b/3$ structure is also a QSH insulator, because we detect edge states at monolayer steps. Our DFT calculations of the $b/3$ structure support this, showing an inverted energy gap at the Y point, opened by spin-orbit coupling, which exchanges the parity between the conduction and valence bands at Y, in full analogy with the conventional $b/2$ structure. The qualitatively identical electronic structure of the $b/2$ and $b/3$ structures is remarkable, as it is known that the stacking order of 2D materials can have a major influence on their electronic and topological properties [33,34]. Here, a massive change in the stacking of the 1D chains in the 2D Bi_4Br_4 plane does not change the topology, which thus turns out to be robust, although both the experimentally determined band gap energy and the DFT calculations with structural parameters derived from the STM experiment consistently indicate that the $b/3$ structure is closer to the transition to a trivial topology than the $b/2$ structure is. Since the monolayer properties of $b/3$ and α-Bi_4Br_4 are almost identical, it is likely that also bulk $b/3$-Bi_4Br_4 is a HOTI. Finally, our observations differ significantly from the structural and electronic properties of α-Bi_4Br_4 under hydrostatic pressure, which has been reported to be metallic/superconducting [29]. The corresponding triclinic unit cell observed at high hydrostatic pressure [29] is also clearly distinct from our observation of AB stacking.

ACKNOWLEDGMENTS

The STM experiment was conducted at the Center for Nanophase Materials Sciences, which is a DOE Office of Science User Facility. F.L. and F.S.T. acknowledge funding from the Bavarian Ministry of Economic Affairs, Regional Development and Energy within Bavaria's High-Tech Agenda Project "Bausteine für das Quantencomputing auf Basis topologischer Materialien mit experimentellen und theoretischen Ansätzen" and Germany's Excellence Strategy-Cluster of Excellence Matter and Light for Quantum Computing (ML4Q). F.L. acknowledges funding by the Deutsche Forschungsgemeinschaft (DFG, German Research Foundation) within the Priority Programme SPP 2244 (Project No. 443416235), as well as the Emmy Noether Programme (Project No. 511561801). J.J.Z. acknowledges support from the National Key R&D Program of China (Grant No. 2022YFA1403400) and the National Natural Science Foundation of China (Grant No. 12104039). Z.W. was supported by the National Key R&D Program of China (No. 2020YFA0308800, and No. 2022YFA1403400), the National Natural Science Foundation of China (No. 92065109), the Beijing National Laboratory for Condensed Matter Physics (Grant No. 2023BNLCMPKF007), and the Beijing Natural Science Foundation (Grant No. Z210006). Z.W. thanks the Analysis & Testing Center at BIT for assistance in facility support.

B.V., F.S.T., and F.L. conceived the experiments. Crystals were grown by Z.W. and Y.Z., J.K.H., H.J., S.M.H., and F.L. conducted the experiments. M.Z. and J.J.Z. performed band structure calculations. T.W. calculated the total energy per unit cell. A.P.L., Y.Y., B.V., F.S.T., and F.L. supervised the project. J.K.H., F.S.T., and F.L. drafted the manuscript and all authors commented on it.

DATA AVAILABILITY

The data that support the findings of this article are openly available [35].

[1] C.-C. Liu, J.-J. Zhou, Y. Yao, and F. Zhang, Weak topological insulators and composite Weyl semimetals: $\beta - Bi_4X_4$ ($X = Br, I$), Phys. Rev. Lett. **116**, 066801 (2016).

[2] J. Han, W. Xiao, and Y. Yao, Quasi-one-dimensional topological material Bi_4X_4 (X = Br,I), Adv. Phys.: X **7**, 2057234 (2022).

[3] S. Yu, J. Deng, W. Liu, Y. Zhang, Y. Sun, N. Dhale, S. Li, W. Ma, Zhuying Wang, P. Wu, Z. Liang, X. Zhang, B. Lv, Zhijun Wang, Zhenyu Wang, and X. Chen, Observation of robust one-dimensional edge channels in a three-dimensional quantum spin Hall insulator, Phys. Rev. X **14**, 041048 (2024).

[4] J.-J. Zhou, W. Feng, C.-C. Liu, S. Guan, and Y. Yao, Large-gap quantum spin Hall insulator in single layer bismuth monobromide Bi_4Br_4, Nano Lett. **14**, 4767 (2014).

[5] J.-J. Zhou, W. Feng, G.-B. Liu, and Y. Yao, Topological edge states in single- and multi-layer Bi_4Br_4, New J. Phys. **17**, 015004 (2015).

[6] X. Peng, X. Zhang, X. Dong, D. Ma, D. Chen, Y. Li, J. Li, J. Han, Z. Wang, C.-C. Liu *et al.*, Observation of topological edge states on α-Bi_4Br_4 nanowires grown on $TiSe_2$ substrates, J. Phys. Chem. Lett. **12**, 10465 (2021).

[7] M. Yang, Yundan Liu, W. Zhou, C. Liu, D. Mu, Yani Liu, J. Wang, W. Hao, J. Li, J. Zhong *et al.*, Large-gap quantum spin Hall state and temperature-induced Lifshitz transition in Bi_4Br_4, ACS Nano **16**, 3036 (2022).

[8] B. A. Bernevig and S.-C. Zhang, Quantum spin Hall effect, Phys. Rev. Lett. **96**, 106802 (2006).

[9] M. S. Lodge, S. A. Yang, S. Mukherjee, and B. Weber, Atomically thin quantum spin Hall insulators, Adv. Mater. **33**, 2008029 (2021).

[10] J. Alicea, New directions in the pursuit of Majorana fermions in solid state systems, Rep. Prog. Phys. **75**, 076501 (2012).

[11] N. Shumiya, M. S. Hossain, J.-X. Yin, Z. Wang, M. Litskevich, C. Yoon, Y. Li, Y. Yang, Y.-X. Jiang, G. Cheng *et al.*, Evidence

of a room-temperature quantum spin Hall edge state in a higher-order topological insulator, Nat. Mater. **21**, 1111 (2022).

[12] C. Yoon, C.-C. Liu, H. Min, and F. Zhang, Quasi-one-dimensional higher-order topological insulators, arXiv:2005.14710.

[13] R. Noguchi, M. Kobayashi, Z. Jiang, K. Kuroda, T. Takahashi, Z. Xu, D. Lee, M. Hirayama, M. Ochi, T. Shirasawa *et al.*, Evidence for a higher-order topological insulator in a three-dimensional material built from van der Waals stacking of bismuth-halide chains, Nat. Mater. **20**, 473 (2021).

[14] W. Zhao, M. Yang, R. Xu, X. Du, Yidian Li, K. Zhai, C. Peng, D. Pei, H. Gao, Yiwei Li *et al.*, Topological electronic structure and spin texture of quasi-one-dimensional higher-order topological insulator Bi_4Br_4, Nat. Commun. **14**, 8089 (2023).

[15] M. S. Hossain, Q. Zhang, Z. Wang, N. Dhale, W. Liu, M. Litskevich, B. Casas, N. Shumiya, J.-X. Yin, T. A. Cochran *et al.*, Quantum transport response of topological hinge modes, Nat. Phys. **20**, 776 (2024).

[16] See Supplemental Material at http://link.aps.org/supplemental/10.1103/tdp5-wmqc for details on the formation of hinge states in α-Bi_4Br_4, the piezo calibration, extended spectroscopy data, and Wilson loop and edge state calculations, which also includes Ref. [17].

[17] Q. Wu, S. Zhang, H.-F. Song, M. Troyer, and A. A. Soluyanov, WannierTools: An open-source software package for novel topological materials, Comput. Phys. Commun. **224**, 405 (2018).

[18] H. von Benda, A. Simon, and W. Bauhofer, Zur Kenntnis von BiBr und $BiBr_{1,167}$, Z. Anorg. Allg. Chem. **438**, 53 (1978).

[19] F. Lüpke, A. D. Pham, Y.-F. Zhao, L.-J. Zhou, W. Lu, E. Briggs, J. Bernholc, M. Kolmer, J. Teeter, W. Ko, C.-Z. Chang, P. Ganesh, and A.-P. Li, Local manifestations of thickness-dependent topology and edge states in the topological magnet $MnBi_2Te_4$, Phys. Rev. B **105**, 035423 (2022).

[20] G. Kresse and J. Furthmüller, Efficient iterative schemes for *ab initio* total-energy calculations using a plane-wave basis set, Phys. Rev. B **54**, 11169 (1996).

[21] J. Heyd, G. E. Scuseria, and M. Ernzerhof, Hybrid functionals based on a screened Coulomb potential, J. Chem. Phys. **118**, 8207 (2003).

[22] A. A. Mostofi, J. R. Yates, Y.-S. Lee, I. Souza, D. Vanderbilt, and N. Marzari, Wannier90: A tool for obtaining maximally-localised Wannier functions, Comput. Phys. Commun. **178**, 685 (2008).

[23] P. Giannozzi, S. Baroni, N. Bonini, M. Calandra, R. Car, C. Cavazzoni, D. Ceresoli, G. L. Chiarotti, M. Cococcioni, I. Dabo *et al.*, QUANTUM ESPRESSO: A modular and open-source software project for quantum simulations of materials, J. Phys.: Condens. Matter **21**, 395502 (2009).

[24] P. Giannozzi, O. Andreussi, T. Brumme, O. Bunau, M. B. Nardelli, M. Calandra, R. Car, C. Cavazzoni, D. Ceresoli, M. Cococcioni *et al.*, Advanced capabilities for materials modelling with QUANTUM ESPRESSO, J. Phys.: Condens. Matter **29**, 465901 (2017).

[25] J. P. Perdew, K. Burke, and M. Ernzerhof, Generalized gradient approximation made simple, Phys. Rev. Lett. **77**, 3865 (1996).

[26] A. Dal Corso, Pseudopotentials periodic table: From H to Pu, Comput. Mater. Sci. **95**, 337 (2014).

[27] S. Grimme, S. Ehrlich, and L. Goerigk, Effect of the damping function in dispersion corrected density functional theory, J. Comput. Chem. **32**, 1456 (2011).

[28] Z. Gong, X. Lai, W. Miao, J. Zhong, Z. Shi, H. Shen, X. Liu, Q. Li, M. Yang, J. Zhuang, and Y. Du, Br-vacancies induced variable ranging hopping conduction in high-order topological insulator Bi_4Br_4, Small Methods **8**2400517 (2024).

[29] X. Li, D. Chen, M. Jin, D. Ma, Y. Ge, J. Sun, W. Guo, H. Sun, J. Han, W. Xiao *et al.*, Pressure-induced phase transitions and superconductivity in a quasi–1-dimensional topological crystalline insulator α-Bi_4Br_4, Proc. Natl. Acad. Sci. USA **116**, 17696 (2019).

[30] S. Tang, C. Zhang, D. Wong, Z. Pedramrazi, H.-Z. Tsai, C. Jia, B. Moritz, M. Claassen, H. Ryu, S. Kahn *et al.*, Quantum spin Hall state in monolayer 1T'-WTe2, Nat. Phys. **13**, 683 (2017).

[31] F. Lüpke, D. Waters, S. C. De La Barrera, M. Widom, D. G. Mandrus, J. Yan, R. M. Feenstra, and B. M. Hunt, Proximity-induced superconducting gap in the quantum spin Hall edge state of monolayer WTe_2, Nat. Phys. **16**, 526 (2020).

[32] C. Murray, C. Van Efferen, W. Jolie, J. A. Fischer, J. Hall, A. Rosch, A. V. Krasheninnikov, H.-P. Komsa, and T. Michely, Band bending and valence band quantization at line defects in MoS_2, ACS Nano **14**, 9176 (2020).

[33] K. Sugawara, N. Yamamura, K. Matsuda, W. Norimatsu, M. Kusunoki, T. Sato, and T. Takahashi, Selective fabrication of free-standing ABA and ABC trilayer graphene with/without Dirac-cone energy bands, NPG Asia Mater **10**, e466 (2018).

[34] F. Lüpke, D. Waters, A. D. Pham, J. Yan, D. G. Mandrus, P. Ganesh, and B. M. Hunt, Quantum spin Hall edge states and interlayer coupling in twisted bilayer WTe_2, Nano Lett. **22**, 5674 (2022).

[35] J. K. Hofmann, H. Jeon, S. M. Hus, Y. Zhang, M. Zheng, T. Wichmann, A.-P. Li, J.-J. Zhou, Z. Wang, Y. Yao, B. Voigtländer, F. S. Tautz, and F. Lüpke, Jülich Data (2025), https://doi.org/10.26165/JUELICH-DATA/KES99Y.